

# The initial mass function of a massive relic galaxy

Ignacio Martín-Navarro<sup>1,2\*</sup>, Francesco La Barbera<sup>3</sup>, Alexandre Vazdekis<sup>1,2</sup>,  
Anna Ferré-Mateu<sup>4</sup>, Ignacio Trujillo<sup>1,2</sup> & Michael A. Beasley<sup>1,2</sup>

<sup>1</sup>*Instituto de Astrofísica de Canarias, E-38200 La Laguna, Tenerife, Spain*

<sup>2</sup>*Departamento de Astrofísica, Universidad de La Laguna, E-38205 La Laguna, Tenerife, Spain*

<sup>3</sup>*INAF - Osservatorio Astronomico di Capodimonte, Napoli, Italy*

<sup>4</sup>*Subaru Telescope, 650 North A'ohoku Place, Hilo, HI 96720, USA*

## ABSTRACT

Massive relic galaxies formed the bulk of their stellar component before  $z \sim 2$  and have remained unaltered since then. Therefore, they represent a unique opportunity to study in great detail the *frozen* stellar population properties of those galaxies that populated the primitive Universe. We have combined optical to near-infrared line-strength indices in order to infer, out to  $1.5 R_e$ , the IMF of the nearby relic massive galaxy NGC 1277. The IMF of this galaxy is bottom-heavy at all radii, with the fraction of low-mass stars being at least a factor of two larger than that found in the Milky Way. The excess of low-mass stars is present throughout the galaxy, while the velocity dispersion profile shows a strong decrease with radius. This behaviour suggests that local velocity dispersion is not the only driver of the observed IMF variations seen among nearby early-type galaxies. In addition, the excess of low-mass stars shown in NGC 1277 could reflect the effect on the IMF of dramatically different and intense star formation processes at  $z \sim 2$ , compared to the less extreme conditions observed in the local Universe.

**Key words:** galaxies: formation – galaxies: evolution – galaxies: elliptical – galaxies: fundamental parameters

## 1 INTRODUCTION

A combination of major and minor dry mergers are the favoured explanation for the evolution of the scaling relations of massive galaxies since  $z \sim 2$  (e.g. Naab et al. 2009; Trujillo et al. 2011; Ferreras et al. 2014; Ruiz et al. 2014). Being a stochastic process, a natural prediction of this evolutionary channel is the presence, in the local volume, of a number of massive galaxies which have experienced few if any significant merger events since they were formed (Quilis & Trujillo 2013). These putative *relic galaxies* present a unique opportunity to study in detail the properties of massive,  $z \sim 2$  galaxy analogues in the nearby Universe.

The Perseus cluster galaxy NGC 1277 fulfills all the characteristics to be considered a relic massive galaxy (Trujillo et al. 2014). The galaxy exhibits an unusually high central velocity dispersion (above  $400 \text{ km s}^{-1}$ ) and is physically compact, with an effective circularized radius of  $1.2 \text{ kpc}$  (Trujillo et al. 2014). The bulk of its stars are old (age  $> 10 \text{ Gyr}$ ) and  $\alpha$ -enhanced ( $[\text{Mg}/\text{Fe}] \sim 0.3 \text{ dex}$ ), which sug-

gests a short ( $\tau \sim 100 \text{ Myr}$ ) and intense ( $\text{SFR} \gtrsim 10^3 \text{ M}_\odot/\text{yr}$ ) star formation burst at  $z \sim 2$ , followed by subsequent quiescent evolution (Trujillo et al. 2014). In addition, NGC 1277 hosts the most massive (compared to the total galaxy mass) black hole found to date (van den Bosch et al. 2012, but see Emsellem 2013).

Trujillo et al. (2014) studied the stellar population properties of NGC 1277 assuming that its stellar initial mass function (IMF) follows that seen in the Milky Way (Kroupa 2002; Chabrier 2003). Although this approach has been extensively used in the literature, many studies (Cenarro et al. 2003; van Dokkum & Conroy 2010; Cappellari et al. 2012; Ferreras et al. 2013; La Barbera et al. 2013; Spiniello et al. 2014) have shown that the shape and the normalization of the IMF correlate with galaxy mass. Moreover, Martín-Navarro et al. (2015) have found that the IMF slope of some representative massive galaxies depends on galactocentric distance. Since the inferred properties of a stellar population strongly depend on the adopted IMF (Ferré-Mateu et al. 2013), it is important to investigate the stellar populations of massive systems such as NGC 1277 while relaxing the assumption of a universal IMF.

The importance of measuring the behaviour of the IMF

\* E-mail: I. Martín-Navarro imartin@iac.es

as a function of radius in NGC 1277 is two-fold. On the one hand, it provides a route to understanding the physical conditions of massive galaxies when the majority of their stars were formed, with no influence from later accretion events. On the other hand, NGC 1277 shows an atypical combination of kinematical and stellar population properties (van den Bosch et al. 2012; Trujillo et al. 2014), which can be used to investigate the main driver behind these IMF variations.

By studying the radial variation of IMF-sensitive spectral indices in NGC 1277, we have been able to derive its IMF radial profile, which remains bottom-heavy up to  $\sim 1.5R_e$ . We have simultaneously inferred, in a self-consistent manner (i.e., by adopting the best-fitting IMF value at each radius), its age, metallicity and [Mg/Fe] gradients. Here we find that the claims made by Trujillo et al. (2014) regarding NGC 1277 as being a relic object are also supported under the assumption of a steep IMF.

This paper is structured as follows: in Section 2 we present our data; Section 3 contains the analysis and the main results, which are finally discussed in Section 4. We adopt a standard cosmology:  $H_0 = 70 \text{ km s}^{-1} \text{ Mpc}^{-1}$ ,  $\Omega_m = 0.3$ , and  $\Omega_\Lambda = 0.7$ .

## 2 DATA AND DATA REDUCTION

Our data consist of two sets of long-slit spectroscopic observations of NGC 1277 carried out at the 4.2m William Herschel Telescope (WHT) and at the 10.4m Gran Telescopio Canarias (GTC), located at the Spanish Observatorio del Roque de los Muchachos on La Palma. The WHT spectra were acquired with the Intermediate dispersion Spectrograph and Imaging System (ISIS), using the R300B grating and a 1 arcsec slit, placed along the major axis of the galaxy (see Trujillo et al. 2014, for details). The total on-source integration time for these observations was 3 hours, with 1 arcsec seeing. The spectra cover the wavelength range from  $\sim 3700$  to  $\sim 6000 \text{ \AA}$ , with  $3.4 \text{ \AA}$  spectral resolution (FWHM). In a second run of observations, we again targeted the NGC 1277 major axis with the GTC Optical System for Imaging and low-Intermediate-Resolution Integrated Spectroscopy (OSIRIS) in order to increase the wavelength coverage up to  $10000 \text{ \AA}$ , allowing us to include near-infrared IMF-sensitive features such as Na 8190 (Schiaffon et al. 2000) and the Calcium triplet (Cenarro et al. 2001). These data have a (wavelength-dependent) resolution ranging from  $6 \text{ \AA}$  at  $\lambda \sim 5000 \text{ \AA}$  to  $8 \text{ \AA}$  at  $\lambda \sim 10000 \text{ \AA}$ . The total exposure time was 1.5 hours on source with a typical  $0.8 \text{ arcsec}$  seeing. In both datasets, the pixel size was  $0.25 \text{ arcsec}$ . In this work, all measurements (i.e. line-strengths indices) blueward and redward of  $5700 \text{ \AA}$  come from WHT and GTC data, respectively.

Data reduction was performed using the REDUCEME package (Cardiel 1999), which allows for the careful treatment of error propagation. The reduction process included the standard bias subtraction, flat-fielding, cosmic ray cleaning, distortion (C and S) correction, wavelength calibration, sky subtraction and flux calibration.

Note that, for our purposes, sky removal is a critical step of the reduction, as both airglow emission and telluric absorption have a prominent role in the raw spectra above

$\lambda \sim 7000 \text{ \AA}$ . To ensure an accurate sky subtraction, an *on-and-off* observational strategy was followed, where the galaxy was offset in the CCD plane during the observations. This allowed for a clean sky emission removal by subtracting consecutive exposures. The second crucial aspect was that of correcting the spectra for telluric absorption features. In order to investigate the impact of such correction on the derived stellar population parameters, we adopted two independent approaches. The spectrophotometric standard star (Hiltner 600, B1) was targeted at the end of the observations. Using the IRAF task *telluric*, the derived atmospheric transmission spectrum was scaled to correct the NGC 1277 data. In addition, we made use of the ESO tool MOLECFIT (Kausch et al. 2014). The latter does not require any extra calibration data (i.e. a spectrophotometric standard star) as it constructs a synthetic atmospheric absorption model for a given spectrum, by fitting spectral regions dominated by telluric absorption in the spectrum itself<sup>1</sup>. To this effect, molecfite relies on the radiative transfer code LBLRTM (Clough et al. 2005), allowing for a simultaneous fit of both the telluric model and the line spread function to the data. The differences in the inferred stellar population properties among the two approaches are described in Appendix A.

Since the analysis of stellar populations requires a higher signal-to-noise (SN) than kinematics, we performed a first radial binning by imposing a SN threshold of 20. The radial velocity and velocity dispersion gradients, derived using the public available software PPXF (Cappellari & Emsellem 2004), are shown in Fig. 1. Our measurements are in good agreement with those published by van den Bosch et al. (2012), showing that NGC 1277 is pressure-supported in the central regions ( $\sigma_c \sim 400 \text{ km s}^{-1}$ ), whereas ordered motions dominate beyond  $\sim 0.5R_e$ . We used the inferred kinematics (radial velocity and velocity dispersion) to correct every row (spectrum) in the image to the rest-frame via linear interpolation of our measurements. Once all the spectra were at rest-frame, we calculated a representative spectrum at each radius of the galaxy with a minimum SN per  $\text{\AA}$  (at  $\lambda\lambda 6000, 6200 \text{ \AA}$ ) of 80 in the outskirts, achieving over 700 in the central bin.

Throughout this work, we assume a circularized effective radius of  $R_e = 1.2 \text{ kpc}$  for NGC 1277, with a  $0.344 \text{ kpc arcsec}^{-1}$  scale (Trujillo et al. 2014). Fig. 2 shows three representative spectra at 0, 0.5, and  $1 R_e$ , respectively. The change in spectral resolution from the WHT to the OSIRIS data appears at  $\lambda = 5700 \text{ \AA}$ . Note also how the intrinsic (associated with the velocity dispersion) resolution varies from the central (in red,  $\sigma \sim 400 \text{ km s}^{-1}$ ) to the outermost bin (in orange,  $\sigma \sim 200 \text{ km s}^{-1}$ ). A zoom around the  $H\beta$  feature is shown as an inset, suggesting no significant contamination of the line from nebular emission (see § 3).

<sup>1</sup> In particular, we run MOLECFIT by fitting the spectral regions  $\lambda\lambda 8130, 8300 \text{ \AA}$ ;  $\lambda\lambda 7585, 7698 \text{ \AA}$ ;  $\lambda\lambda 7235, 7326 \text{ \AA}$  and  $\lambda\lambda 6861, 6924 \text{ \AA}$ , where strong  $H_2O$  and  $O_2$  telluric features are found.

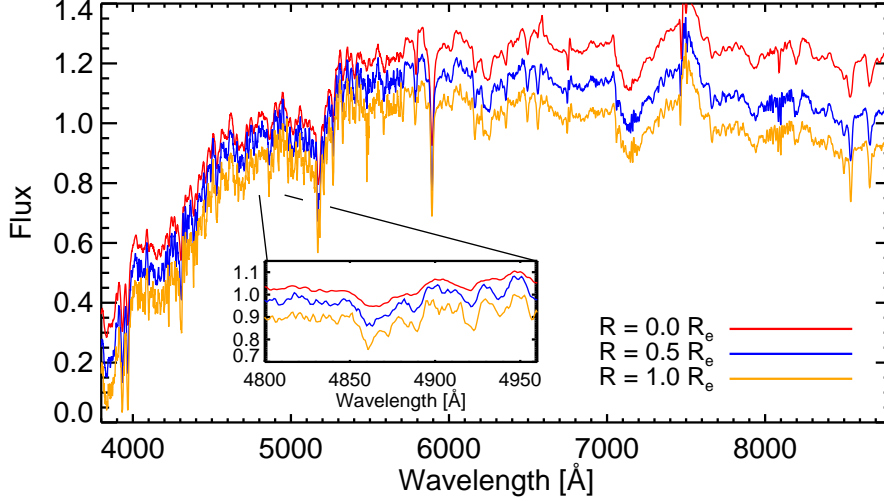


**Figure 2.** Averaged spectra at 0.0 (red), 0.5 (blue) and 1.0 (yellow)  $R_e$ , arbitrarily scaled in the vertical direction. Note the different spectral resolution between the GTC-OSIRIS ( $\lambda > 5700$  Å) and the WHT ( $\lambda < 5700$  Å) data. Note also the large variation in the velocity dispersion, reflected in a gradual smoothing when moving from the outer 1.0 $R_e$  spectrum to the central radial bin. The inset panel shows a zoom in of the  $H\beta$  line.

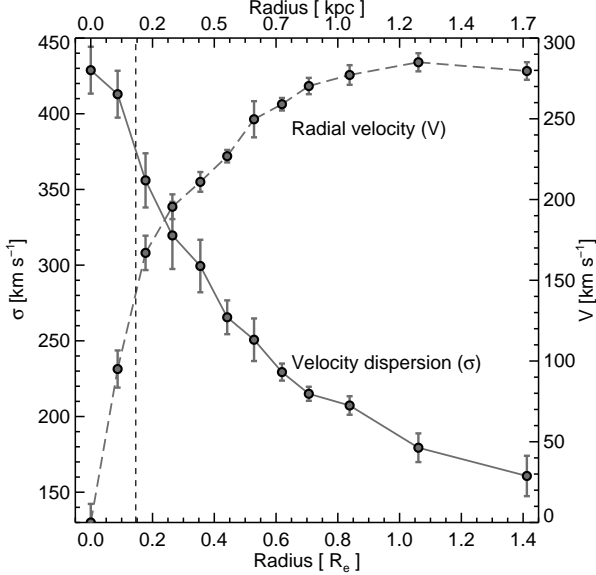


**Figure 1.** Velocity dispersion (solid line, left vertical axis) and radial velocity (dashed line, right vertical axis) profiles as a function of the major-axis radial distance, normalized to the (circularized) effective radius  $R_e$ . Dashed vertical line indicates the seeing radius, measured by its average half width at half maximum (HWHM) value (0.4 arcsec).

### 3 ANALYSIS AND RESULTS

We based our stellar population analysis on the extended version of the MILES models (Vazdekis et al. 2010, 2012). The MILES models cover a range from  $-2.32$  dex to  $+0.22$  dex in total metallicity, and from 0.06 Gyr to 17 Gyr in age. We assumed a bimodal IMF, parametrised as a two-segment function (Vazdekis et al. 1996), where the star number per logarithmic mass bin is given by:

$$\phi(\log m) \stackrel{\text{def}}{=} \frac{d\mathcal{N}}{d \log m} \propto \begin{cases} m_p^{-\Gamma_b} & m \leq 0.2 M_\odot \\ p(m) & 0.2 M_\odot < m \leq 0.6 M_\odot \\ m^{-\Gamma_b} & m > 0.6 M_\odot \end{cases}$$

where  $m_p$  determines the turning-point mass, set to  $m_p = 0.4 M_\odot$  in the Vazdekis et al. (2010, 2012) models.  $p(m)$  is a spline function satisfying a set of boundary conditions so that  $\phi(m)$  is continuous:

$$\begin{aligned} p(0.2 M_\odot) &= m_p^{-\Gamma_b} \\ p'(0.2 M_\odot) &= 0 \\ p(0.6 M_\odot) &= 0.6^{-\Gamma_b} \\ p'(0.6 M_\odot) &= -\Gamma_b 0.6^{-(\Gamma_b+1)} \end{aligned}$$

We allowed for a variation in the IMF slope,  $\Gamma_b$ , from 0.8 (bottom-light) to 3.3 (bottom-heavy). Under this parametrisation, the standard Kroupa-like IMF is well represented by a slope of  $\Gamma_b = 1.3$ . Note that  $\Gamma_b$  varies the slope of the high-mass end of the (bimodal) IMF, in contrast to other studies where the high-mass end of the IMF is kept fixed, while the low-mass end is varied (e.g. Conroy & van Dokkum 2012). Since the (bimodal) IMF is normalized to have a total mass of  $1 M_\odot$ , changing  $\Gamma_b$  does actually vary the mass fraction of low- to high-mass stars. Hence, for the present study,  $\Gamma_b$  should not be regarded as the high-mass end slope of the IMF, but rather as a proxy for the fraction of low-mass stars.

To determine the stellar population parameters we followed the same approach as in La Barbera et al. (2013). Age, metallicity, and IMF slope were obtained by minimising the following equation:

$$\chi^2(\Gamma_b, \text{age}, [Z/H]) = \sum_i \left[ \frac{(EW_i - \Delta_{\alpha,i}) - EW_{M,i}}{\sigma_{EW_i}} \right]^2, \quad (1)$$

where the sum expands over the  $i$ th observed and predicted line-strength indices included in the analysis.  $EW_i$  are the measured line-strengths,  $EW_{M,i}$  the predictions from MILES models, and  $\Delta_{\alpha,i}$  is a correction applied to each index to account for deviations from a non-solar abundance scale, and the effect of “residual” abundance ratios on line strengths (see La Barbera et al. 2013 and Appendix A, for details). To derive  $[Mg/Fe]$ , for each radial bin we estimated separately the Magnesium and the Iron metallicities ( $Z_{Mg}$  and  $Z_{Fe}$ , respectively) through index-index fitting of the  $H_{\beta_o}$  vs. Mgb and  $\langle Fe \rangle$  line-strengths, respectively. We then subtracted one metallicity from the other to calculate the  $[Z_{Mg}/Z_{Fe}]$  proxy, which tightly correlates with the “true”  $[Mg/Fe]$  (see Fig.6 in La Barbera et al. 2013). In Fig. 3 we show the measured radial profiles of all indices considered in the fitting process, along with the best-fitting SSP solution at each radius. Notice that the  $H_{\beta_o}$  line has been corrected for nebular emission contamination, as detailed in Appendix A.

The derived age, metallicity and  $[Mg/Fe]$  radial profiles are shown in Fig. 4. NGC 1277 exhibits a flat age profile, always above 10 Gyrs. The metallicity, on the contrary, decreases with increasing radius. Notice that the metallicity in the central bin (+0.41 dex) exceeds the maximum value of MILES models (+0.22). Hence, for this specific bin, we extrapolated the models (in the same way as in La Barbera et al. 2013) to match the observed indices (in particular, the total metallicity indicator  $[MgFe]'$ ). Although in general there is a good agreement between the observed and best-fitting line strengths in Fig. 3, some discrepancies exist. In particular, the mismatch between observed and model indices in the most central bins (see, e.g., panels (f) and (i)), can be at least partly understood as a limitation of the stellar population models to describe very metal-rich ( $\gtrsim 0.2$  dex) populations and/or uncertainties in the age estimate. However, none of these issues significantly affect the results of our work, as discussed in Appendix A. Fig. 4 also shows that the  $[Mg/Fe]$  gradient of NGC 1277 is flat, with  $[Mg/Fe] \sim 0.3$  dex at all radii. This flat  $[Mg/Fe]$  radial profile can be also directly inferred from the fact that both the Mgb and  $\langle Fe \rangle$  spectral indices (see panels (a) and (b) of Fig. 3) show a similar amount of radial variation<sup>2</sup>. Note that the large error bars on  $[Mg/Fe]$  in the central regions reflect the uncertainties on the  $[Fe/H]$  and  $[Mg/H]$  determination/extrapolation used to derive the  $[Mg/Fe]$  proxy. The gradients shown in Fig. 4 are in agreement with those published by Trujillo et al. (2014, Fig. 4 in their paper). This is not a trivial result, since here we have allowed for possible radial variations of the IMF.

The IMF radial profile of NGC 1277 is shown in Fig. 5, where the shaded region accounts for the scatter among  $\Delta\Gamma_b$  values from different tests, where the fitting process

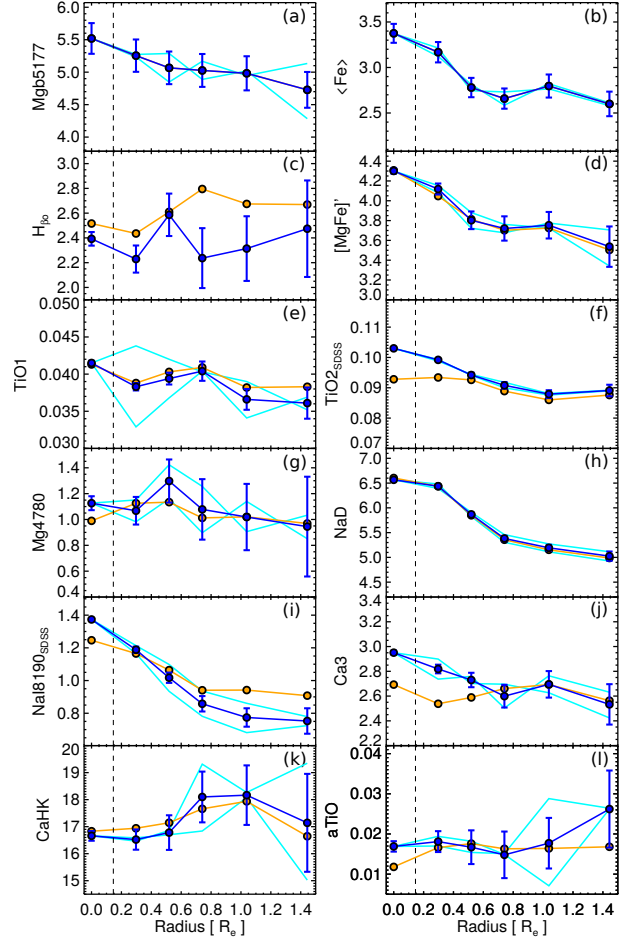


**Figure 3.** Observed gradients of the age-, metallicity- and IMF-sensitive indices considered in the fitting process (blue symbols). Dark blue represents the mean radial profile, whereas in light blue we show the radial gradient at each side of the galaxy. The  $1\sigma$  error bars are also shown for the mean profile. The best-fitting solution is overplotted in orange. The definition of all spectral indices are given in La Barbera et al. (2013), while aTiO has been computed according to the definition of Spiniello et al. (2014). Although not individually included in the fitting process, panels (a) and (b) show the Mgb and  $\langle Fe \rangle$  line-strength profiles. Note that, according to the MILES models, both indices have quite similar sensitivities to a variation in total metallicity. Since they also exhibit the same radial variation ( $\sim 0.8\text{\AA}$ ), a flat  $[Mg/Fe]$  gradient is expected, consistent with Fig. 4. In all panels, dashed vertical lines mark the seeing radius.

has been repeated with different sets of spectral indices and different methods to remove telluric lines as detailed in Appendix A. Regarding the discrepancies between the observed and best-fitting line strengths (see Fig. 3), note that the  $TiO_2$  and  $NaI8190$  lines can be potentially affected by errors in the flux calibration (the former) and telluric residuals (both). Although the central  $TiO_2$  value might suggest a slightly steeper IMF profile, our best-fitting solution points to a mild radial variation of IMF slope ( $\Gamma_b \sim -0.5$ ), i.e. a bottom-heavy IMF at all radii. Notice that in the present analysis we have not included the  $CaH1$ <sup>3</sup> and  $CaH2$  IMF-

<sup>2</sup> Notice, in fact, that in MILES models, both Mgb and  $\langle Fe \rangle$  have a similar sensitivity to total metallicity, hence a similar radial gradient for the two indices implies a flat trend of the  $[Z_{Mg}/Z_{Fe}]$  proxy.

<sup>3</sup> Although not used in our analysis, the radial variation of the

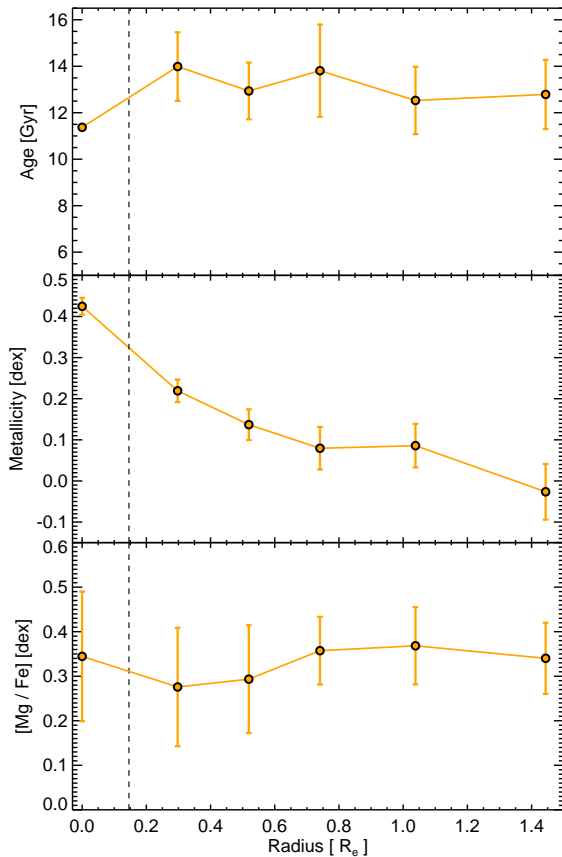


**Figure 4.** Best-fitting age (top), metallicity (middle) and  $[\text{Mg}/\text{Fe}]$  (bottom) gradients. Both age and  $[\text{Mg}/\text{Fe}]$  show a fairly flat radial behaviour, whereas metallicity decreases by 0.4 dex from the centre outwards to  $1.5R_e$ . An extrapolation of stellar population models is required to account for line-strength values in the central region. In all panels, dashed vertical lines mark the seeing radius.

sensitive features of Spiniello et al. (2015), as (1) CaH1 has been shown to be not matched by extended MILES models (regardless of the IMF, see La Barbera et al. 2013), while (2) CaH2 is strongly affected by the  $\text{O}_2$  ( $B$ -band) atmospheric absorption at  $\lambda \sim 6900 \text{ \AA}$  in our data. Concerning Ca3, the (observed) index tends to decrease with radius, while our best-fitting solutions favour a flat radial behaviour for Ca3. This discrepancy might be related to some radial variation of the  $[\text{Ca}/\text{Fe}]$  abundance ratio which is not well captured by our fitting approach. In fact, although we have included  $[\text{Ca}/\text{Fe}]$  as a free fitting parameter (see Appendix A), the  $[\text{Ca}/\text{Fe}]$  is mainly constrained, in this work, from the CaHK line, which is strongly affected by the abundance pattern of other alpha elements (e.g. Vazdekis et al. 2015). Nevertheless, a decreasing trend of Ca3 with radius is the opposite behaviour to what one would expect for a less bottom-heavy IMF at larger radii (as Ca3 decreases with  $\Gamma_b$ ). This is consistent with our conclusion that the IMF of NGC1277 shows only a mild radial variation. In fact, as shown in Appendix A,

CaH1 index is mild (0.002 mag) further supports a rather flat IMF profile.

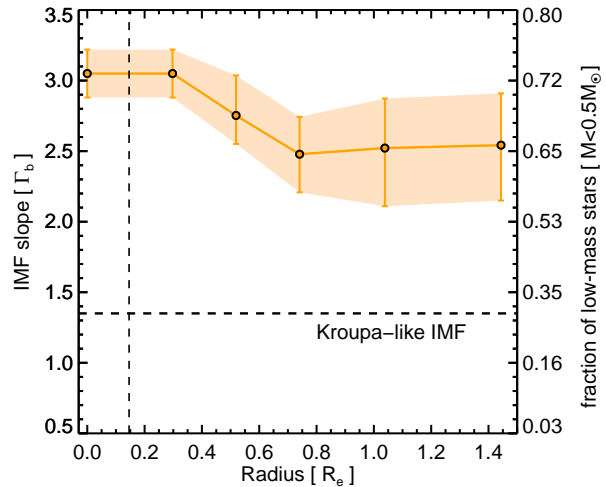


**Figure 5.** Radial IMF-slope gradient for the relic massive galaxy NGC 1277. The left vertical axis indicates the slope of the IMF in the bimodal case ( $\Gamma_b$ ), i.e., the slope of the IMF for stars with masses larger than  $0.5M_\odot$ . This  $\Gamma_b$  parameter can be transformed into a dwarf-to-giant ratio (right vertical axis), which is what the line-strength indices are actually tracing (La Barbera et al. 2013). For reference, the Milky-Way IMF value is shown as a horizontal dashed line. The inferred IMF gradient is mildly decreasing and it is very bottom-heavy up to  $1.5R_e$ . Uncertainties (the orange shaded region) are obtained by removing line-strength indices from the fitting process which might be potentially affected by flux calibration, telluric correction or modelling uncertainties. Dashed vertical line indicates the extent of the seeing disc.

removing this index altogether from the fits does not significantly change the radial trend of  $\Gamma_b$ . Regarding aTiO, the only point that deviates significantly from the best-fits is the innermost one. This could be related to some issue in the extrapolation of the models at high metallicity, and/or some peculiar abundance ratio for  $R=0R_e$ . However, as the deviation affects only one single point, it does not change our general conclusions about the radial behaviour of  $\Gamma_b$  for NGC1277.

The robustness of the IMF profile, against all issues mentioned so far, is demonstrated in Appendix A, where we show how the mildly decreasing behaviour of  $\Gamma_b$  persists under different telluric correction procedures (see § 2), as well as different combinations of indices included in the fits, and changes in the modelling assumptions.

Ultimately, gravity-sensitive indices trace the dwarf-to-giant star ratio in the IMF, regardless of the adopted IMF parametrization (La Barbera et al. 2013). This is explicitly shown in the right vertical axis of Fig. 5, where we represent the fraction (in mass) of stars below  $0.5M_\odot$  for each IMF slope. The inferred dwarf-to-giant ratio in NGC 1277 is, at all radii, at least a factor of 2 larger than in the Milky Way (horizontal dashed line).

The inferred stellar population properties of NGC 1277 (ages, metallicities, and IMF slopes; as shown in Figs. 4 and 5) can be used to estimate the stellar M/L radial profile. Notice, however, that for old stellar systems ( $\gtrsim 10$  Gyr), stellar population analysis cannot provide fully reliable mass-to-light ratios, as it relies on the assumption of a given parametrisation for the IMF (Ferreras et al. 2014). In

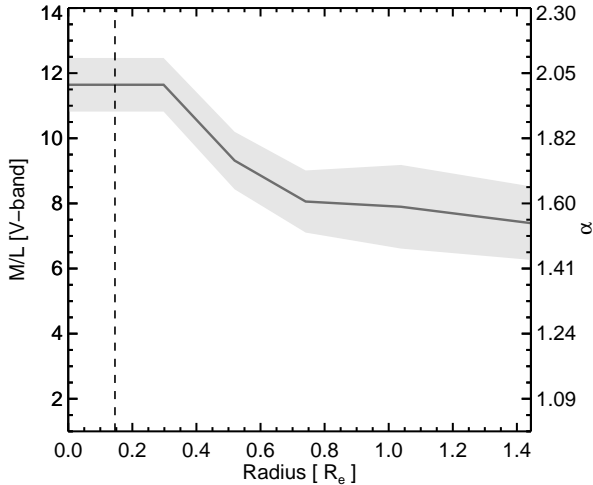


**Figure 6.** Radial M/L ratio (V-band) gradient for the massive compact galaxy NGC 1277, under the assumption of a bimodal IMF. At each radius, the best-fitting age, metallicity and IMF slope shown in Figs. 4 and 5 translate into a V-band M/L ratio. The right-hand axis represents the “mismatch parameter”,  $\alpha$ , defined as the ratio between the inferred M/L and that expected from a stellar population with the same age and metallicity as observed, but with a Milky Way-like IMF slope. Notice that the absolute values of the M/L gradients heavily depend on the parametrisation adopted for the IMF (Ferreras et al. 2014). The light shaded region accounts for the uncertainties in all the stellar population parameters (e.g., error bars in Fig. 4 and shaded region in Fig. 5). Dashed vertical lines mark the seeing radius.

this sense, our favoured bimodal distribution seems to better match the dynamical M/L estimates (La Barbera et al. 2013; Spiniello et al. 2014), while a single power-law distribution provides unrealistically high M/L’s. For a bimodal IMF parametrisation, the expected M/L radial profile of NGC 1277 is shown in Fig. 6.

## 4 DISCUSSION

### 4.1 The excess of low-mass stars in ETGs

What drives the excess of low-mass stars in ETGs remains unknown, however there are presently two distinct candidates, namely [Mg/Fe] and  $\sigma$ . The latter may be viewed as a dynamical controlling parameter, whereas the former is a stellar population parameter.

Dynamical studies (Treu et al. 2010; Cappellari et al. 2012) suggest that the galaxy central velocity dispersion correlates strongly with the IMF slope - with more massive galaxies having steeper IMF slopes than less massive galaxies. This result has found support from several groups using different methodologies (Ferreras et al. 2013; La Barbera et al. 2013; Spiniello et al. 2014). However, based on our analysis, we *reject the hypothesis that local velocity dispersion is the principal agent driving IMF variations*. Given the velocity dispersion gradient observed in NGC 1277 (from  $\sim 420 \text{ km s}^{-1}$  to  $150 \text{ km s}^{-1}$ ), if the correlation between IMF slope and central velocity dispersion holds also for local velocity dispersion, we would expect a typical radial change in the IMF slope of  $\Delta\Gamma_b = -2.4$ .

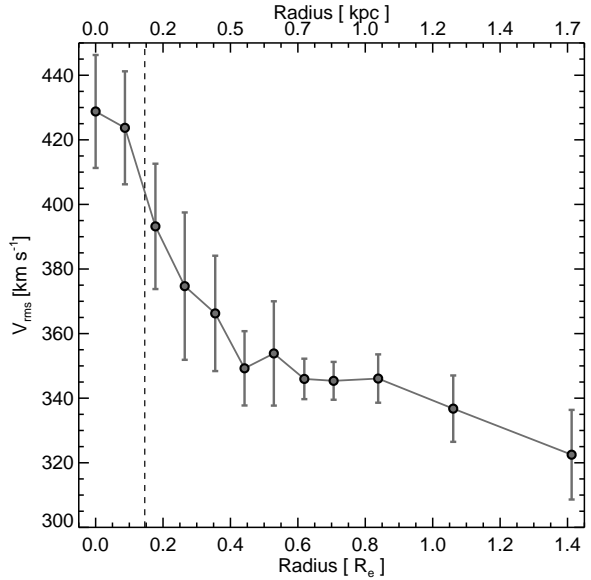


**Figure 7.** Radial  $V_{\text{rms}}$  profile of NGC 1277. This quantity, accounting for the total kinetical energy, is more closely related to the effective velocity dispersion, which has been found to tightly correlate with the observed IMF variations. The radial  $V_{\text{rms}}$  variation is significant, albeit milder, than the  $\sigma$  variation. Dashed vertical lines mark the seeing radius.

This value is incompatible with our inferred IMF gradient ( $\Delta\Gamma_b \sim -0.5$ ). Note, however, that our conclusions apply to the local velocity dispersion, not to the effective central velocity dispersion. To investigate the relation between IMF slope and local kinematical properties of NGC 1277, we show in Fig. 7 its  $V_{\text{rms}}$  radial profile, defined as:

$$V_{\text{rms}} = \sqrt{V_{\text{rot}}^2 + \sigma^2}$$

Note that the effective velocity dispersion analysed in La Barbera et al. (2013) and in Spiniello et al. (2014), which was estimated using a 3 arcsec wide fibre, is better represented by  $V_{\text{rms}}$  rather than by the local sigma, since the latter does not include the line broadening associated with the rotational velocity profile. Both  $\Gamma_b$  and  $V_{\text{rms}}$  decrease with radius;  $V_{\text{rms}}$  is greater than  $300 \text{ km s}^{-1}$ , and  $\Gamma_b$  is steeper than the Milky Way value at all radii in NGC 1277. This is consistent with previous works reporting a bottom-heavy IMF at high *effective* velocity dispersion.

As an alternative explanation for the IMF variations, based on stellar population analysis, Conroy & van Dokkum (2012) found that the IMF slope also correlates with the overabundance of  $\alpha$ -elements, in particular with the [Mg/Fe] ratio, in the sense that galaxies more enhanced in [Mg/Fe] have steeper IMF slopes. As we mentioned in §3, our [Mg/Fe] measurements are heavily dependent on the interpolation scheme we use, and we find that our data can entertain either slightly decreasing or increasing [Mg/Fe] radial gradients. Therefore, from the present study we cannot assess the relation between IMF slope and [Mg/Fe] (but see La Barbera et al. 2015).

To understand the differences among the aforementioned studies, Smith (2014) has independently reviewed the dynamical results from Cappellari et al. (2012) and those based on stellar population analysis of Conroy & van Dokkum (2012). Although he found an overall agreement between both studies, the galaxy-by-galaxy comparison shows that the correlation between IMF slope and velocity dispersion does not agree with that found when comparing the IMF and  $[\text{Mg}/\text{Fe}]$ .

The rapidly growing observational evidence of a variable IMF slope may be in tension with other well-established properties of ETGs in the local Universe. In particular, chemical evolution models assuming a bottom-heavy IMF are unable to reproduce the observed metallicities and abundance ratios of ETGs (Arrighi et al. 2010). This idea has been recently revisited in a series of articles by Weidner et al. (2013) and Ferreras et al. (2015) (see also Vazdekis et al. 1997; Larson 1998) who found that a time-dependent IMF is necessary to explain the stellar population properties of massive ETGs at  $z \sim 0$ . Note that, according to Ferreras et al. (2015), a constant-in-time IMF can be ruled out, not only for a bimodal IMF shape, but also for a two-segment IMF parametrization (e.g. as defined in Conroy & van Dokkum 2012), and even for a V-shaped IMF (characterized by an enhanced fraction of both low- and high-mass stars).

## 4.2 The emerging picture

Our analysis of the stellar population properties of NGC 1277 is summarized in Figs. 4 and 5. The radial age profile of this galaxy, even allowing for possible IMF variations, indicates that the underlying stellar population is very old ( $\gtrsim 10$  Gyr) at all radii, with no evidence of recent star formation (Trujillo et al. 2014). This result suggests that the stellar component of NGC 1277 was formed at high redshift ( $z \gtrsim 2$ ), and that solving for the IMF at each radius does not convert NGC 1277 into a young, massive and compact system, as those identified in the local Universe (Trujillo et al. 2009; Ferré-Mateu et al. 2012, 2013).

In terms of kinematics, NGC 1277 shows an extreme radial velocity dispersion gradient, ranging from more than  $400 \text{ km s}^{-1}$  in the centre to  $\sigma \sim 150 \text{ km s}^{-1}$  beyond  $1 \text{ Re}$ . The rotation in this galaxy shows the opposite behaviour, rising to  $V_{\text{rot}} \sim 280 \text{ km s}^{-1}$  at  $1 \text{ Re}$ . Interestingly, these differences in the kinematical properties between the centre and the outskirts of NGC 1277 are not reflected in the properties of its stellar populations. The radial variation of  $\alpha$ -element overabundance, age and IMF slope are mild, whereas the total metallicity decreases by  $\sim 0.4$  dex from the centre to  $1 \text{ Re}$ . These gradients are consistent with a *fast, monolithic-like formation process* (Sánchez-Blázquez et al. 2007). In this sense, in terms of its stellar population properties, NGC 1277 does not differ from typical massive ETGs in the Local Universe. However, its extreme dynamics and compact morphology set it apart from the vast majority of local ETGs.

The IMF radial profile of NGC 1277 further constrains the formation process of massive ETGs. NGC 1277 shows much weaker radial variations of the IMF slope ( $\Delta\Gamma_b = -0.5$ ) when compared to the IMF gradient of the two massive galaxies analysed by Martín-Navarro et al. (2015)

( $\Delta\Gamma_b = -1.5$ ). Our suggestion is that NGC 1277 represents the monolithic-like formation phase of massive ETGs. In this picture the later accretion of less massive satellites (with “standard” Kroupa-like IMF slopes), which would settle preferentially in the galaxy periphery due to their lower densities, would steepen the pristine IMF gradient making it more similar to that found in nearby massive galaxies Martín-Navarro et al. (2015).

Indeed, we hypothesize that relic galaxies, such as NGC 1277, will evolve to become the cores of massive ellipticals in the nearby Universe (Trujillo et al. 2014). The bulk of the stellar mass of this galaxy was formed in a short ( $\tau \sim 100$  Myr) and intense ( $\text{SFR} \gtrsim 10^3 \text{ M}_\odot/\text{yr}$ ) burst at redshift  $z \gtrsim 2$ , but remained concentrated within a few kpc in the centre of the dark matter halo. Afterwards, through dry merging (van Dokkum et al. 2010; Trujillo et al. 2011; Ferreras et al. 2014), the system would typically evolve to the characteristic sizes and stellar masses that are observed at  $z \sim 0$ . This interpretation is supported by numerical simulations (e.g. Oser et al. 2010; Navarro-González et al. 2013), and also by stellar population studies of the outskirts of nearby ETGs (Coccato et al. 2010; La Barbera et al. 2012; Pastorello et al. 2014; Montes et al. 2014). Since dry mergers cannot significantly alter the properties of the stellar populations, a relic massive galaxy should present the same stellar population properties as the core of a typical  $z \sim 0$ , massive ETG, but with the latter’s morphology and kinematics shaped by successive mergers.

It may seem surprising, at face value, that such a relic system should be identified in such a dense and dynamic environment such as that represented by the Perseus cluster ( $M_{200} = 7.74 \times 10^{14} \text{ M}_\odot$ , Aleksić et al. 2010). However, this is in fact a natural expectation in the hierarchical clustering paradigm since overdensities in what are now galaxy clusters were the first structures to collapse and to form massive galaxies (Mo & White 1996). In addition, the active intracluster environment may have inhibited the subsequent formation of younger stellar populations within NGC 1277 either via the stripping or heating of cold gas (Edge et al. 1992; O’Dea et al. 2008). In this sense, Stringer et al. (2015) have recently shown that in the BOLSHOI numerical simulation (Klypin et al. 2011), dark matter haloes similar to those hosting NGC 1277-like objects have experienced below-average mass accretion, or even mass loss, since  $z = 2$ .

Finally, we find that the radial IMF behaviour seen in NGC 1277 is not driven by the local velocity dispersion, and therefore, it cannot explain the IMF variations seen in ETGs. The fact that the IMF slope can vary radially within galaxies (Martín-Navarro et al. 2015) suggests a complex galaxy formation scenario, with significantly different enrichment and supernovae-feedback rates when comparing the centre and the outskirts of ETGs. Thus, more observational efforts are needed to better understand the IMF behaviour in nearby galaxies, investigating what stellar population properties can explain the observed IMF variations. In this sense, large resolved spectroscopic surveys such as CALIFA (Sánchez et al. 2012) and MaNGA will provide statistically significant samples. In addition, the joint analysis of the IMF inferred from dynamical modelling and from stellar population analysis can reveal important information about the interplay between galaxy stellar population properties and dynamics. The intrinsic degeneracies of these methods



( $M/L$  ratios, dark matter content, stellar remnants and central black-hole mass) may be broken if both approaches are combined.

**Acknowledgements** We thank Ignacio Ferreras for his insightful comments and suggestions on the paper. Also, we would like to thank the two anonymous referees for their precise and constructive suggestions. We acknowledge support from the Spanish Government grant AYA2013-48226-C3-1-P. Based on observations made with the WHT and the GTC telescopes, both installed in the Spanish Observatorio del Roque de los Muchachos of the Instituto de Astrofísica de Canarias.

## REFERENCES

- Aleksić J. et al., 2010, *ApJ*, 710, 634  
 Arrigoni M., Trager S. C., Somerville R. S., Gibson B. K., 2010, *MNRAS*, 402, 173  
 Cappellari M., Emsellem E., 2004, *PASP*, 116, 138  
 Cappellari M. et al., 2012, *Nature*, 484, 485  
 Cardiel N., 1999  
 Cenarro A. J., Cardiel N., Gorgas J., Peletier R. F., Vazdekis A., Prada F., 2001, *MNRAS*, 326, 959  
 Cenarro A. J., Gorgas J., Vazdekis A., Cardiel N., Peletier R. F., 2003, *MNRAS*, 339, L12  
 Cervantes J. L., Vazdekis A., 2009, *MNRAS*, 392, 691  
 Chabrier G., 2003, *PASP*, 115, 763  
 Clough S. A., Shephard M. W., Mlawer E. J., Delamere J. S., Iacono M. J., Cady-Pereira K., Boukabar S., Brown P. D., 2005, *Journal of Quantitative Spectroscopy and Radiative Transfer*, 91, 233  
 Coccatto L., Gerhard O., Arnaboldi M., 2010, *MNRAS*, 407, L26  
 Conroy C., van Dokkum P. G., 2012, *ApJ*, 760, 71  
 Edge A. C., Stewart G. C., Fabian A. C., 1992, *MNRAS*, 258, 177  
 Emsellem E., 2013, *MNRAS*, 433, 1862  
 Ferré-Mateu A., Vazdekis A., de la Rosa I. G., 2013, *MNRAS*, 431, 440  
 Ferré-Mateu A., Vazdekis A., Trujillo I., Sánchez-Blázquez P., Ricciardelli E., de la Rosa I. G., 2012, *MNRAS*, 423, 632  
 Ferreras I., La Barbera F., de la Rosa I. G., Vazdekis A., de Carvalho R. R., Falcón-Barroso J., Ricciardelli E., 2013, *MNRAS*, 429, L15  
 Ferreras I. et al., 2014, *MNRAS*, 444, 906  
 Ferreras I., Weidner C., Vazdekis A., La Barbera F., 2015, *MNRAS*, 448, L82  
 Kausch W. et al., 2014, in *Astronomical Society of the Pacific Conference Series*, Vol. 485, *Astronomical Data Analysis Software and Systems XXIII*, Manset N., Forshay P., eds., p. 403  
 Klypin A. A., Trujillo-Gomez S., Primack J., 2011, *ApJ*, 740, 102  
 Kroupa P., 2002, *Science*, 295, 82  
 La Barbera F., Ferreras I., de Carvalho R. R., Bruzual G., Charlot S., Pasquali A., Merlin E., 2012, *MNRAS*, 426, 2300  
 La Barbera F., Ferreras I., Vazdekis A., 2015, *MNRAS*, 449, L137  
 La Barbera F., Ferreras I., Vazdekis A., de la Rosa I. G., de Carvalho R. R., Trevisan M., Falcón-Barroso J., Ricciardelli E., 2013, *MNRAS*, 433, 3017  
 Larson R. B., 1998, *MNRAS*, 301, 569  
 Martín-Navarro I., Barbera F. L., Vazdekis A., Falcón-Barroso J., Ferreras I., 2015, *MNRAS*, 447, 1033  
 Mo H. J., White S. D. M., 1996, *MNRAS*, 282, 347  
 Montes M., Trujillo I., Prieto M. A., Acosta-Pulido J. A., 2014, *MNRAS*, 439, 990  
 Naab T., Johansson P. H., Ostriker J. P., 2009, *ApJL*, 699, L178  
 Navarro-González J., Ricciardelli E., Quilis V., Vazdekis A., 2013, *MNRAS*, 436, 3507  
 O’Dea C. P. et al., 2008, *ApJ*, 681, 1035  
 Oser L., Ostriker J. P., Naab T., Johansson P. H., Burkert A., 2010, *ApJ*, 725, 2312  
 Pastorello N., Forbes D. A., Foster C., Brodie J. P., Usher C., Romanowsky A. J., Strader J., Arnold J. A., 2014, *MNRAS*, 442, 1003  
 Quilis V., Trujillo I., 2013, *ApJL*, 773, L8  
 Ruiz P., Trujillo I., Mármol-Queraltó E., 2014, *MNRAS*, 442, 347  
 Sánchez S. F. et al., 2012, *A&A*, 538, A8  
 Sánchez-Blázquez P., Forbes D. A., Strader J., Brodie J., Proctor R., 2007, *MNRAS*, 377, 759  
 Schiavon R. P., Barbuy B., Bruzual A. G., 2000, *ApJ*, 532, 453  
 Smith R. J., 2014, *MNRAS*, 443, L69  
 Spiniello C., Trager S., Koopmans L. V. E., Conroy C., 2014, *MNRAS*, 438, 1483  
 Spiniello C., Trager S. C., Koopmans L. V. E., 2015, *ApJ*, 803, 87  
 Stringer M., Trujillo I., Dalla Vecchia C., Martínez-Valpuesta I., 2015, *MNRAS*, 449, 2396  
 Treu T., Auger M. W., Koopmans L. V. E., Gavazzi R., Marshall P. J., Bolton A. S., 2010, *ApJ*, 709, 1195  
 Trujillo I., Cenarro A. J., de Lorenzo-Cáceres A., Vazdekis A., de la Rosa I. G., Cava A., 2009, *ApJL*, 692, L118  
 Trujillo I., Ferré-Mateu A., Balcells M., Vazdekis A., Sánchez-Blázquez P., 2014, *ApJL*, 780, L20  
 Trujillo I., Ferreras I., de la Rosa I. G., 2011, *MNRAS*, 415, 3903  
 van den Bosch R. C. E., Gebhardt K., Gültekin K., van de Ven G., van der Wel A., Walsh J. L., 2012, *Nature*, 491, 729  
 van Dokkum P. G., Conroy C., 2010, *Nature*, 468, 940  
 van Dokkum P. G. et al., 2010, *ApJ*, 709, 1018  
 Vazdekis A., Casuso E., Peletier R. F., Beckman J. E., 1996, *ApJS*, 106, 307  
 Vazdekis A. et al., 2015, *MNRAS*, 449, 1177  
 Vazdekis A., Peletier R. F., Beckman J. E., Casuso E., 1997, *ApJS*, 111, 203  
 Vazdekis A., Ricciardelli E., Cenarro A. J., Rivero-González J. G., Díaz-García L. A., Falcón-Barroso J., 2012, *MNRAS*, 424, 157  
 Vazdekis A., Sánchez-Blázquez P., Falcón-Barroso J., Cenarro A. J., Beasley M. A., Cardiel N., Gorgas J., Peletier R. F., 2010, *MNRAS*, 404, 1639  
 Weidner C., Ferreras I., Vazdekis A., La Barbera F., 2013, *MNRAS*, 435, 2274

## APPENDIX A: ROBUSTNESS OF THE INFERRED IMF PROFILE

To check the reliability of the IMF gradient of NGC 1277 (Fig. 5), we have explored three possible sources of systematics, namely, errors on telluric absorption correction, the effect of non-solar elemental abundances, and the nebular emission contamination to the  $H_{\beta_0}$  line. These tests – supporting the robustness of our results – have been performed because of some discrepancies between the best-fitting and observed line-strengths (see Sec. 3), in particular regarding the  $H_{\beta_0}$ , Ca and Na spectral lines (see panels (c), (i) and (j) of Fig. 3).

The fact that the best-fitting  $H_{\beta_0}$  lies above the observed values (panel (c) in Fig. 3) may indicate some residual contamination from nebular emission to the line profile. In the present work, the nebular emission correction to  $H_{\beta_0}$  has been estimated in a self-consistent manner (see La Barbera et al. 2013 for details), i.e., for each IMF slope ( $\Gamma_b$ ) explored in the fitting process, we apply the correction calculated by simultaneously fitting the  $H_{\beta}$  line



profile with a 2 SSP model (for a given  $\Gamma_b$ ) plus a gaussian emission line. For the two innermost radial bins, the correction turned out to be fully consistent with zero regardless of  $\Gamma_b$ , while in the bins from  $\sim 0.5$  to  $1.5 R_e$ , a mild correction was found<sup>4</sup>, in the range from 0.1 to 0.2 Å. Therefore, it is unlikely that differences in panel (c) of Fig. 3 are due to residual nebular contamination. Note also that underestimating  $H_{\beta_o}$  (in particular for the outermost bins) would imply that, given the age sensitivity of the TiO features, the inferred IMF slope is shallower than the “true” one, hence strengthening our conclusion about a shallow IMF gradient in NGC 1277. The possible explanation for the mismatch between the best-fitting and observed  $H_{\beta_o}$  may reside in the uncertainty of the stellar population models used to account for non-solar abundance ratios on line strengths (in particular  $H_{\beta_o}$ ). We modelled deviations from solar partition with the semi-empirical approach described in La Barbera et al. (2013), with the further aid of the Conroy & van Dokkum (2012, hereafter CvD) stellar population models. In practice, the  $\Delta_{\alpha,i}$  terms in Eq. 3 can be expanded as follows (see §3.3 in Martín-Navarro et al. 2015):

$$\Delta_{\alpha,i} = C_{\alpha,i} \cdot [\alpha/\text{Fe}] + \Delta_{X,i} \cdot \delta X$$

where  $C_{\alpha,i}$  is the observed sensitivity of the  $i$ -th index to  $[\alpha/\text{Fe}]$  (derived from SDSS stacked spectra, as in La Barbera et al. 2013);  $\Delta_{X,i}$  is the theoretical sensitivity of each index to the abundance ratio of a specific element X, estimated with CvD models, and  $\delta X$  is a “residual” abundance of element X, not accounted for by the  $C_{\alpha,i}$  correction, and treated as a fitting parameter. In other terms, we remove the bulk dependence of each index on  $[\alpha/\text{Fe}]$  with the  $C_{\alpha,i}$  terms, while still allowing for some residual abundance effect on the indices through the best-fitting  $\delta X$ ’s. In practice, following La Barbera et al. 2013, we have considered only the effect of elemental abundances of selected gravity-sensitive features, i.e.  $X = \text{Ca}, \text{Na}, \text{and Ti}$ . Regarding  $H_{\beta_o}$ , we have  $\Delta X \sim 0$  for all X’s but  $X = \text{Ti}$ , i.e. CvD models predict a significant sensitivity of  $H_{\beta_o}$  to  $[\text{Ti}/\text{Fe}]$  abundance ratio (in the sense of  $H_{\beta_o}$  increasing with  $[\text{Ti}/\text{Fe}]$ ). In fact, we found that the  $[\text{Ti}/\text{Fe}]$  tends, on average, to increase the best-fitting  $H_{\beta_o}$  by  $\sim 0.15\text{Å}$ , possibly explaining at least part of the observed mismatch between the best-fitting<sup>5</sup> and observed  $H_{\beta_o}$  in panel (c) of Fig. 3. Since the dependence of  $H_{\beta_o}$  on specific elemental abundances may be significantly affected by theoretical uncertainties on stellar population models (see Cervantes & Vazdekis 2009), we have repeated the fitting process by (i) removing the  $\Delta_{\text{Ti},H_{\beta_o}} \cdot \delta\text{Ti}$  term from Eq. 3, and (ii) excluding the  $H_{\beta_o}$  index altogether from the fits. The resulting IMF profiles from these tests are plotted in Fig. A1, showing no significant differences with respect to the reference profile in Fig. 5. Moreover, neglecting the  $[\text{Ti}/\text{Fe}]$  effect on  $H_{\beta_o}$  leads to a better agreement between observed and best-fitting radial trends for this line, as shown in Fig. A2.

As mentioned in § 2, one major issue in constraining the IMF is the removal of telluric lines from the observed spectra. In the present work, we have removed atmospheric absorption with two independent approaches, i.e., (1) using a spectrophotometric standard star and (2) applying the software MOLECFIT. Fig. A1 compares the corresponding IMF best-fitting profiles, showing no significant differences within the uncertainties. The two approaches lead to an estimated IMF radial variation of (1)  $\Delta\Gamma_b = -0.5$  and (2)  $\Delta\Gamma_b = -0.6$ , respectively.

To further explore to what extent the mismatch of Ca and Na lines for some radial bins (see panels (i) and (j) of Fig. 3) may be affecting our conclusions, we have recomputed the IMF

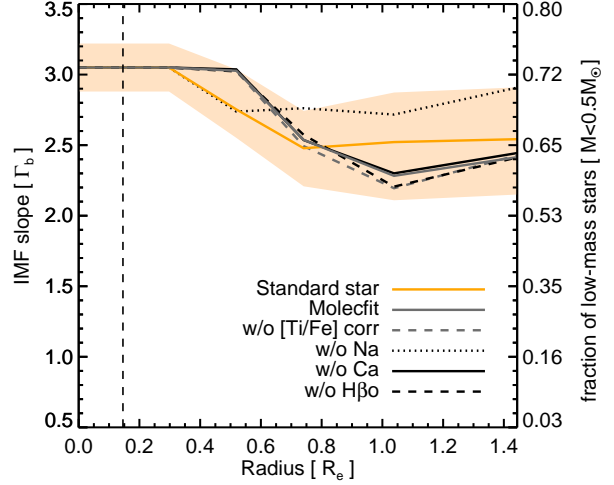


**Figure A1.** Same as Fig. 5 but including tests to check the robustness of our IMF inference. The gray solid line indicates the IMF profile obtained using Molecfit to correct telluric absorption, whereas the gray dashed line corresponds to the best-fitting solution if the  $[\text{Ti}/\text{Fe}]$  dependence of  $H_{\beta_o}$  ignored. In solid black, dotted and dashed lines we show the IMF profile when excluding from the fitting the Calcium, Sodium and  $H_{\beta_o}$  features, respectively. The overall agreement among all the fits shows that our main result is not significantly affected by telluric, nebular emission or model uncertainties. Dashed vertical lines mark the seeing radius.

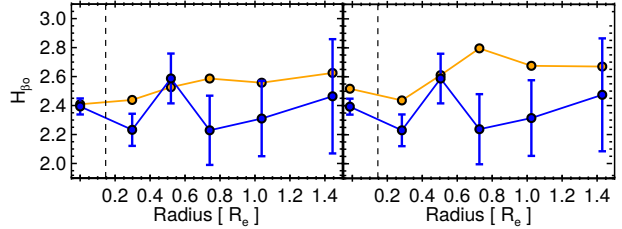


**Figure A2.** Observed and best-fitting  $H_{\beta_o}$  radial profiles. The right panel is the same as panel (c) in Fig. 3, whereas the left panel corresponds to the case where  $[\text{Ti}/\text{Fe}]$  abundance effects on  $H_{\beta_o}$  are neglected. Notice, in the latter case, the better agreement between best-fitting and observed indices, with no significant impact on the inferred IMF profile (Fig. A1).

profile by excluding, as we did for  $H_{\beta_o}$  (see above), all Na and Ca lines in turn, from the fitting procedure. Again, the resulting IMF gradients, shown in Fig. A1, are compatible with the IMF profile reported in Fig. 5. It is worth noting that the impact of removing Na lines is the most significant, suggesting either some residual telluric contamination in the data, or some model uncertainties in dealing with the abundance ratios (Spiniello et al. 2015).

All the above tests, summarized in Fig. A1, indicate that our IMF inference is robust against *i)* nebular emission correction, *ii)* abundance effects (on  $H_{\beta}$  line), *iii)* age determination through  $H_{\beta_o}$  itself, *iv)* telluric correction, and *v)* the set of lines included in the analysis.

<sup>4</sup> Notice that this correction is already applied to observed  $H_{\beta_o}$  values (blue dots) in Fig. 3.

<sup>5</sup> Note that the best-fitting indices in Fig. 3 are actually given by  $\text{EW}_{M,i} + \Delta_{\alpha,i}$ .